Published in partnership with CECCR at King Abdulaziz University

https://doi.org/10.1038/s41612-026-01426-4

Equatorward shift of marine heatwaves centroids in the Atlantic Ocean

Xuanliang Ji[1,2,3,4], Juan Feng[3,4] ✉, Jianping Li[5,6], Xingrong Chen[1,2], Fred Kucharski[7], Xichen Li[8] & Ruiqiang Ding[9]

Ocean warming intensifies marine heatwaves (MHW) globally, increasing their frequency, intensity, duration, and extent, threatening marine ecosystems and economies. However, the latitudinal redistribution of MHW remains unquantified. Analyzing multisource data (1982–2023), we reveal a striking equatorward shift of MHW centroids (MHWC) at an average rate of ~1° latitude per decade across the northern and southern Atlantic basins, implying more frequent MHW in lower latitudes. This equatorial shift lacks seasonal phase-locking and is linearly independent of interannual climate variabilities known to influence the Atlantic variations. Mechanism analysis reveals that the Atlantic MHWC shift originates from the interplay between amplified tropical atmosphere-ocean positive feedbacks, which involve sea surface temperature, sea level pressure, and cloud-radiative interactions, and the concurrent weakening of equatorial and coastal upwelling. The attribution analysis shows anthropogenic warming is the dominant driver of this equatorward trend. The observed shift and rising MHW exposure in lower latitudes underscore the necessity for enhanced modeling fidelity at the regional scale, as this shift would worsen biodiversity loss and extreme events.

Marine heatwave (MHW) refers to prolonged episodes of anomalous high sea surface temperature (SST) during which SST values consistently surpass climatological thresholds over an extended period[1]. These extreme oceanic events have triggered widespread ecological disasters, including coral bleaching[2–6], fisheries collapse[7–9], and biodiversity loss[10–12]. Additionally, MHW can influence weather patterns by enhancing oceanic latent heat release. For instance, elevated SST anomalies (SSTA) provide additional energy input, intensifying tropical hurricanes and prolonging their lifecycle[13–15]. Moreover, MHW can adjust the atmosphere-ocean energy exchange, resulting in European summer heatwaves[16] and severe winter drought[17]. With the rise in global mean temperatures, a series of extreme MHW events has been observed over the Atlantic. Notable examples include the MHW events over the northern Atlantic (NA) in 2012[18], the southwest Atlantic in 2013–14[19] and the southwestern Atlantic in 2017[20]. The frequency, duration, and intensity of Atlantic MHWs have shown significant upward trends[21–23]. Climate projections indicate this trend will intensify with continued anthropogenic ocean warming[23,24], potentially amplifying risks to marine biodiversity and critical ecosystem services that sustain coastal economies and food security[25]. Thus, understanding the characteristics of MHWs is essential for improving climate forecasting accuracy and mitigating the significant socioeconomic impacts linked to these extreme events.

MHW originates from localized heat flux anomalies driven by coupled atmosphere-ocean dynamics. Climate variabilities play a significant role in determining the formation of global MHW events[16,26–30]. El Niño-Southern Oscillation (ENSO) events generate pan-Pacific MHW via anomalous easterlies and thermocline deepening[31]. Moreover, ENSO mediates trans-basin atmospheric teleconnections that weaken Atlantic trade winds, driving eastward-propagating downwelling Kelvin waves that create favorable oceanic conditions for MHW development[32]. Atlantic Niño (ATL3) events amplify MHW persistence over the southern Atlantic (SA) via wind-evaporation-SST feedback sustained by anomalous easterlies[33]. Besides, anomalous circulation patterns and feedback processes also have significant impacts on the occurrence and formation of MHW. Persistent high-pressure systems enhance solar radiation and suppress turbulent cooling through reduced wind mixing[33–35]. In contrast, MHW in the Western

[1]State Key Laboratory of Satellite Ocean Environment Dynamics, National Marine Environmental Forecasting Center, Beijing, China. [2]Key Laboratory of Research on Marine Hazards Forecasting, Ministry of Natural Resources, Beijing, China. [3]State Key Laboratory of Remote Sensing Science, Faculty of Geographical Science, Beijing Normal University, Beijing, China. [4]Beijing Engineering Research Center for Global Land Remote Sensing Products, Faculty of Geographical Science, Beijing Normal University, Beijing, China. [5]Frontiers Science Center for Deep Ocean Multi-spheres and Earth System/Key Laboratory of Physical Oceanography/ Academy of the Future Ocean, Ocean University of China, Qingdao, China. [6]Laoshan Laboratory, Qingdao, China. [7]Abdus Salam International Centre for Theoretical Physics, Trieste, Italy. [8]Institue of Ocean Research, Peking University, Beijing, China. [9]Faculty of Geographical Science, Beijing Normal University, Beijing, China. ✉e-mail: fengjuan@bnu.edu.cn

Boundary Current regions is mainly dominated by warm water advection, and mesoscale eddies drive rapid variations in SST[36,37]. Heat budget analyses confirm that the initiation of MHW is connected with increased shortwave radiation and reduced evaporation, whereas termination aligns with enhanced turbulent dissipation[31]. Additionally, the positive cloud-SST feedback serves as an important amplifier that prolongs and intensifies MHW events[38,39].

Earlier studies on the spatiotemporal characteristics of MHW events mainly focused on their frequency, intensity, extent, and duration[22,29,30,33,40,41]. While numerous studies have mapped the global distribution of MHWs, quantitative analyses of the spatiotemporal migration of MHW centroids (MHWC), especially at the basin scale, are still lacking. Here, the MHWC for a given year and basin is defined as the frequency-weighted mean latitude of all MHW events, representing the geographical center of MHW events. This resolves the gap in understanding how the geographical centers of MHW activity are changing. Meanwhile, the Atlantic basin has witnessed a pronounced poleward migration of tropical cyclone tracks[42] and a significant equatorward shift of the Intertropical Convergence Zone[43]. These changes in large-scale circulations dynamically reconfigure circulation circumstances, convective heat transfer efficiency, and atmosphere-ocean feedback processes. Through their synergistic interactions, these processes establish synoptic-scale thermodynamic architectures that govern MHW initiation and spatiotemporal propagation patterns. Consequently, such dynamical adjustments may drive corresponding shifts in MHWC. Thus, what are the observed changes in the MHWC across the Atlantic basin in recent decades, and what underlying physical mechanisms govern the changes? Here, we integrate multisource satellite observations and Coupled Model Intercomparison Project Phase 6 (CMIP6) simulations to quantify the characteristics of Atlantic MHWC (60°S-60°N), encompassing tropical, mid-latitude, and Western Boundary Current regions, to mitigate the impact of sea ice coverage. We identify a significant equatorward shift of Atlantic-averaged MHWC, demonstrating its thermodynamic linkage to the changes in atmosphere-ocean processes. Critically, detection and attribution analyses confirm that this equatorward shift primarily stems from anthropogenic greenhouse gas forcing.

Results

Observed Equatorward shift of MHWC over the Atlantic

Using two observational datasets, global daily remotely sensed National Oceanic and Atmospheric Administration (NOAA) Optimum Interpolation SST (OISST) V2 and Operational Sea Surface Temperature and Ice Analysis (OSTIA) (**Observational products in Methods**) from 1982 to 2023, Atlantic MHW frequency is calculated (**Definition of MHWs in Methods**). To align with the seasonal cycles of the NA and SA basins, we define a year as the period from March of the current year to February of the following year. (**Annual and Seasonal Definitions for Atlantic in Methods**). Consequently, the study period for observational data spans the 41 complete years from 1982 to 2022, providing continuous data support for the trend analysis.

Both datasets reveal consistent climatological patterns and spatial distribution in the trends of MHW frequency. The annual-mean MHW frequency ranges from 0.99 to 3.74 events per year (Supplementary Fig. 1A), with higher values in the tropical eastern Atlantic (TEA) and the Western Boundary Current regions and their extensions (WBCE), including the Gulf Stream (GS) and the Brazil-Malvinas Confluence (BRZ), consistent with prior studies[33]. The notable increase in MHW frequency within the WBCE is likely driven by several factors, like the intensification of these currents[44,45], enhanced mesoscale eddy activity[36], meridional heat content transport[46], enhanced net ocean heat uptake[47]. The convergence of these factors highlights that in regions with sharp SST gradients like the WBCE, dynamical perturbations in current intensity and path can effectively translate into substantial local warming, making these hotspots highly susceptible to frequent MHW events. Conversely, the increased MHW frequency in the TEA is strongly correlated with a negative phase of the North Atlantic Oscillation (NAO)[33] and heat flux convergence by mean flows[36]. Specifically, the suppression of surface evaporative cooling by weakened trade winds, combined with oceanic heat convergence, leads to rapid heat accumulation in the Atlantic tropical upper ocean[48] and the subsequent triggering of MHW events. Moreover, the meridional distribution of zonal-mean MHW frequency demonstrates a spatial pattern reflective of its climatological distribution, marked by three distinct peaks extending from south to north (Supplementary Fig. 1B). These peaks are predominantly localized in the BRZ, TEA, and GS regions, respectively.

Similarly, the increasing trends in Atlantic MHW frequency across these regions significantly surpass those in other areas, particularly within the GS region and the TEA region (Fig. 1). The increase trend in zonal-averaged MHW frequency in these two regions exceeds 1 count per decade, with the TEA exhibiting a faster rate of increase compared to the GS region. Conversely, MHW frequency exhibits a decline in certain regions of the southern Atlantic, notably in the extra-tropics and the southeastern region of Argentina, with reductions of up to 1.5 counts per decade. This spatial heterogeneity manifests as a multi-polar structure characterized by several regional peaks, reflecting the diverse and localized physical drivers influencing MHW dynamics across the basin. Similar non-uniform distribution has been observed in the trends of MHW frequency over the past century[41,49]. Furthermore, the spatial patterns of changes in MHW frequency align with the observed trends of SST during the same period (Supplementary Fig.e 2), supporting the fact that the observed trends in MHW frequency are primarily driven by mean SST warming[41].

To further verify the robustness of these spatial shifts and address the observed multi-polar complexity, we performed a supplementary analysis of area-weighted mean trends across three representative latitudinal bands in each hemisphere: tropic (0°-10°), mid-latitude (25°-35°), and high-latitude (50°-60°). A definitive latitudinal gradient is observed in MHW intensification (Supplementary Fig. 3). Specifically, the trend rate in the tropic band is markedly higher than that in the high-latitude band in the NA, while high-latitude trends in the SA remain relatively small or even statistically insignificant. Consequently, the spatiotemporal characteristics of MHW frequency indicate a disproportionately stronger increasing trend in the tropical Atlantic compared to higher latitudes. This latitudinal disparity proposed the hypothesis for the meridional shifts of the basin-wide, zonal-mean MHWC.

Figure 2 demonstrates a pronounced equatorward shift of Atlantic MHWC in both NA and SA basins. Specifically, the MHWC represents a frequency-weighted spatial centroid, reflecting the integrated geographic focus of MHW occurrences across the basin rather than the location of absolute maximum SST anomalies or peak intensity. The annual-mean MHWC in the NA spans latitudes from 37.95°N to 24.41°N, while those in the SA range from 41.42°S to 26.96°S. Both of them exhibit statistically significant alignment in the changes of annual-mean MHWC latitude between datasets (Supplementary Table 1) demonstrating robust inter-source coherence in capturing MHWC variations. Although discrepancies emerge in the exact shift rates, the combined hemispheric shift rates align closely, with a total rate of -21.57 ± 9.02 km/year. Additionally, by averaging the two estimates of the MHWC latitudes, the results illustrate an equatorward shift at a rate of approximately 1° latitude per decade. This suggests a higher increase in frequency of MHW events in the lower-latitude Atlantic Ocean compared to the higher-latitude regions. Further, this equatorward shift is observed across all seasons, with unanimous negative slopes detected regardless of seasonal variations in shift rates (Fig. 2B, D, F). This consistency demonstrates that the equatorward shift shows non-significant seasonally dependence, suggesting it is not likely driven by seasonal phase-locking climate variabilities[50,51]. Additionally, sensitivity analysis confirms that the equatorward migration remains robust to latitudinal weighting (Supplementary Figure 4), which only marginally increases the migration rate (e.g., from −23.32 ± 9.60 to −24.36 ± 9.85 km yr^{-1} in OISST), showing a negligible impact on the overall trend magnitude and significance.

To further verify the robustness of the finding, we conducted 4 additional sensitivity definitions by varying MHW thresholds, climatological base periods, and datasets (**Definition of MHW in Methods**;

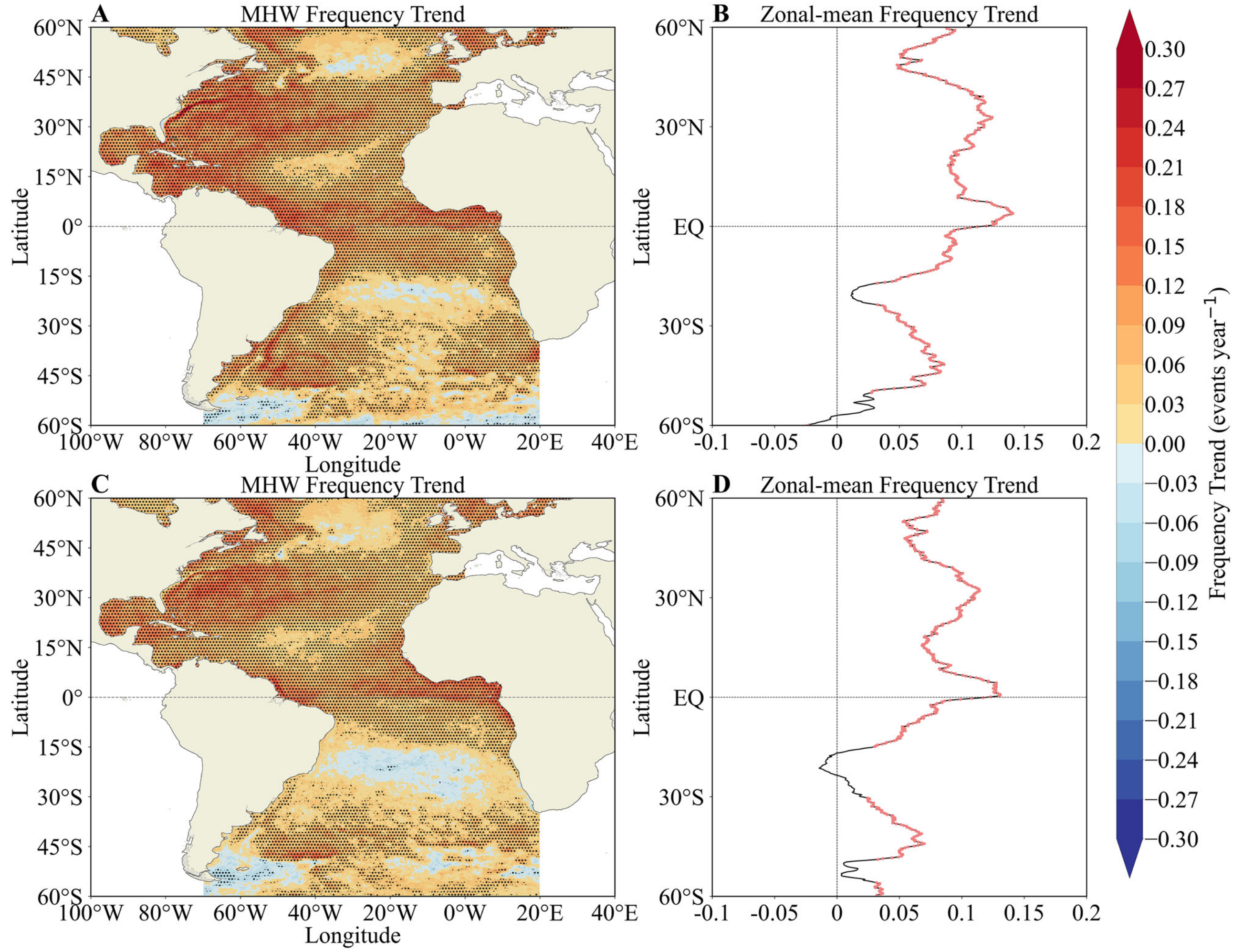

Fig. 1 | Trends in marine heatwave (MHW) frequency. **A** Spatial distribution of trends of the annual-mean MHW frequency over period 1982–2022 based on the OISST. Black dots indicate trends significant at the 0.1 significance level, based on a two-sided Student's *t*-test. **B** Meridional distribution of zonal-mean trends of MHW frequency from the OISST. The zonal mean was calculated using grid cell area weighting to ensure accurate spatial averaging. Red dots indicate trends significant at the 0.1 significance level, based on a two-sided Student's *t*-test. **C, D:** As (**A**) and (**B**), but for the results from the OSTIA.

Supplementary Table 2; Supplementary Figs. 5, 6). Across all 32 independent cases, the observed equatorward shift remains exceptionally coherent, with 100% of the calculated trends exhibiting negative values. While the amplitude of shift during individual seasons may be affected by certain internal variabilities, the robustness of this equatorward shift is confirmed by the 20 models under CMIP6 historical simulations (Supplementary Table 3). The 20-model ensemble mean reveals a highly significant equatorward migration ($p < 0.1$) across all seasons (Supplementary Fig. 7), supporting that the observed MHWC shift is a physically based phenomenon. To elucidate the mechanisms driving this hemispherical synchronized shift, subsequent analyses will focus on integrated hemispheric MHWC changes.

Earlier studies have established linkages between MHW frequency and interannual-to-decadal climate variabilities. For instance, ENSO influences tropical Atlantic wind fields via Pacific–Atlantic teleconnections, triggering regional MHW[26]. ATL3 events prolong SA MHW duration via equatorial easterly wind anomalies[33]. And the intensified occurrence of MHW in the TEA exhibits a robust linkage to the negative phase of NAO, highlighting the dominant role of large-scale variabilities in modulating regional MHW activity[33,52]. We conduct lead-lag correlation analyses to examine the relationships between these three climate indices (**Climate indices in Methods**) and MHWC latitude (Supplementary Fig. 8). The results reveal distinct phase-dependent linkages: ENSO exhibits a negative correlation with MHWC latitude at a 4-month lead ($r = -0.40$, $p < 0.01$), NAO shows a positive correlation at zero lag ($r = 0.35$, $p < 0.01$), and ATL3 demonstrates a robust negative correlation at a 4-month lead ($r = -0.59$, $p < 0.01$), demonstrating that these variabilities exert potential impacts on the MHWC latitude. Correspondingly, we further focus on the impacts of preceding-winter ENSO and ATL3, concurrent NAO on the trend of MHWC latitude (Fig. 3). The equatorward shift of Atlantic MHWC remains robust after removing the linear effects of these climate variabilities, indicating that these modes exert no dominant control over the observed equatorward shift (Fig. 3A, C, E).

We further assess the impacts of positive and negative phases of three climate variabilities on the MHWC latitude. Although the MHWC tends to shift equatorward (poleward) during El Niño (La Niña) events, these ENSO-related displacements are not statistically significant relative to the climatological baseline ($p > 0.1$, *ns* as shown in Fig. 3B). Comparatively, the ATL3 and NAO phases exert a more discernible influence. Specifically, both positive and negative phases of ATL3 are associated with statistically significant latitudinal anomalies in the OISST and OSTIA datasets (Fig. 3F). And negative NAO phases insignificantly favor equatorward MHWs positioning (Fig. 3D), aligning with reported elevated MHW occurrence in the tropical Atlantic during NAO-negative regimes[33,52]. Consequently, while the NAO and ATL3 indices exert some influence on interannual scales, they lack significant long-term trends and therefore cannot account for the

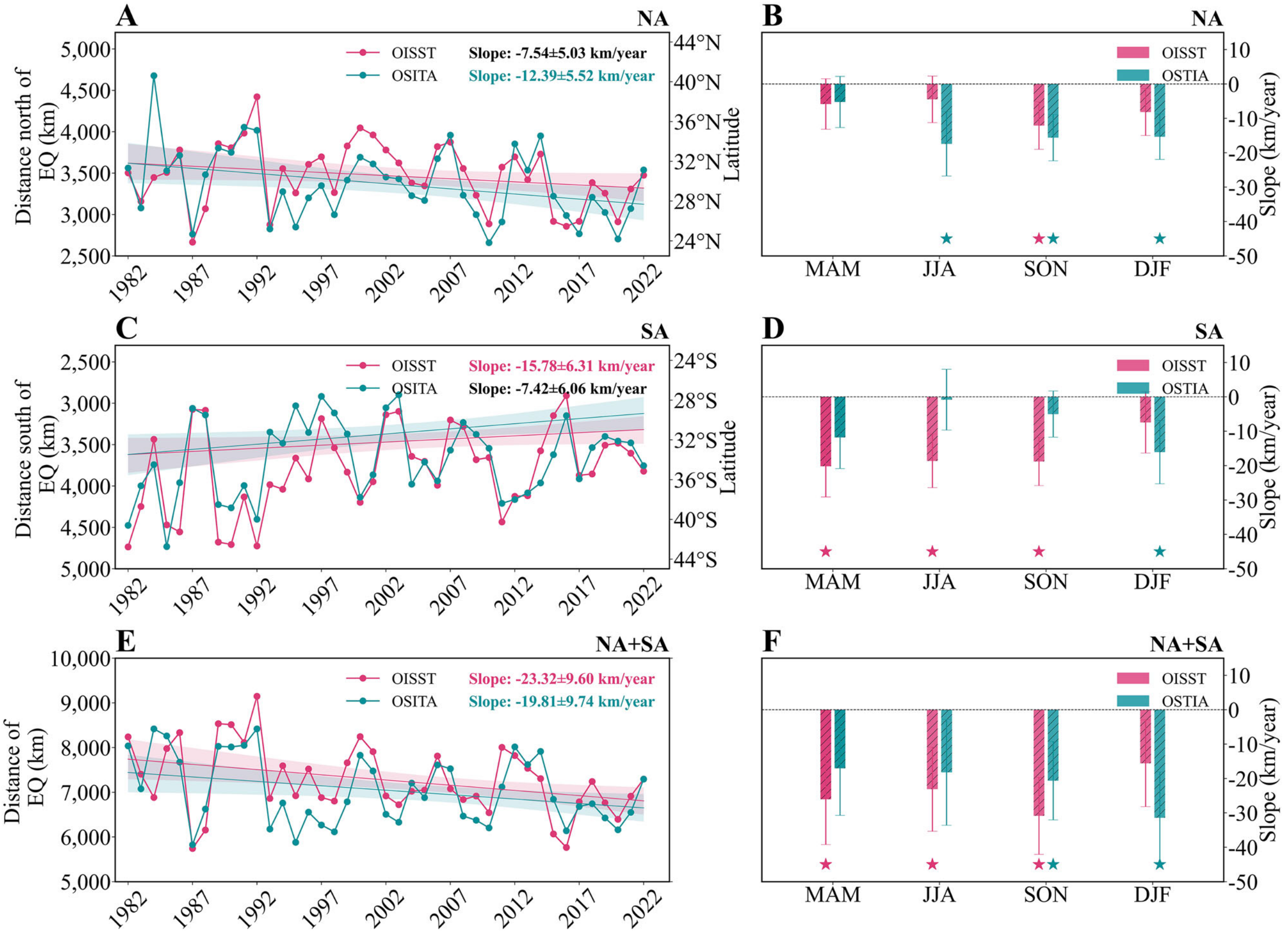

Fig. 2 | Equatorward shift of the latitude of MHW centroids (MHWC) in the Atlantic during period 1982-2022. A Dotted time series of annual-mean latitude of MHWC calculated from the OISST (red line) and OSTIA (green line) in the northern Atlantic (NA, 0°-60°N). The solid line denotes the corresponding linear trends with their slopes shown in the upper right corner. Negative slopes represent equatorward shift. The linear trends, calculated using the Theil-Sen estimator, are shown as solid lines. The corresponding slope values (km per year) in the upper right corner are displayed in color (red/green) if the trend is statistically significant ($p < 0.1$, Student's t-test and Mann-Kendall test); otherwise, they are shown in black. **B** Trends of seasonal-mean latitude of MHWC in the NA based on the OISST (red bars) and OSTIA (green bars), respectively. Blue star denotes trends significant at the 0.1 significance level, based on a two-sided Student's t-test and Mann-Kendall test analysis. **C**, **D** and **E**, **F:** As **A**, **B**, but for the results in the southern Atlantic (SA, 60°S-0°) and combined hemispheric domain (NA + SA, 60°S-60°N), respectively. The y-axis in **C** increases downwards. The confidence interval in the linear regression (shading in **A**, **C**, **E**) is estimated as 90% of linear regression values after performing a bootstrap replacement procedure to the observed MHWL data (using 10000 iterations).

observed MHWC shift trend. Moreover, the potential role of these climate variabilities on the trends of MHWC latitude is verified by using a quadratic regression and a threshold-based extreme event approach (Supplementary Fig. 9). Notably, the statistically significant and asymmetric anomalies observed during extreme ATL3 and NAO phases indicate that these variabilities can indeed exert a modulating influence on the interannual fluctuations of MHWC latitude, however, they do not alter the observed trend of equatorward displacement in the Atlantic over recent decades.

Additionally, decadal climate variabilities, such as the Atlantic Multidecadal Oscillation (AMO), Pacific Decadal Oscillation (PDO), and Interdecadal Pacific Oscillation (IPO), can significantly modulate Atlantic SST patterns[18,30,33]. Nonetheless, their impacts on Atlantic SSTs often exhibit pronounced regional heterogeneity and spatial asymmetry[18]. Specifically, the inherently antisymmetric influence of these modes on SSTs over the NA versus the SA suggests they are unlikely candidates for driving the synchronized long-term MHWC trends. Nevertheless, potential contributions from internal climate variabilities at interdecadal and longer timescales cannot be ruled out; however, it remains difficult to quantify the magnitude of such impacts using limited-duration observational records. Subsequent analysis will disentangle natural forcing from anthropogenic contributions to quantify the relative roles of internal climate variability and human activity in shaping MHWC trends.

Physical drivers of Equatorward shift in MHWC latitude

Prior studies have established that atmosphere-ocean feedback mechanisms, like the longwave radiation flux (LWF)-sea level pressure (SLP)-high-level cloud cover (HCC)-SST coupling, play a pivotal role in amplifying and sustaining SSTA across tropical ocean basins[53–55]. Warm SSTAs are associated with low-pressure anomalies, enhance convective high-level clouds formation, reduce longwave heat loss, and thereby reinforce the SSTA. This feedback mechanism has been implicated in anomalous SST over the Atlantic Warm Pool[56] and AMO-driven tropical Pacific warming[55]. While LWF is a critical mediator, the total net surface heat flux represents the direct thermodynamic driver for upper-ocean heat content. A distinct and significant increasing trend in the net heat flux within the equatorial and tropical Atlantic, particularly in the central-eastern basin (Supplementary Fig. 10). This net energy gain at the ocean surface provides a direct and positive thermodynamic contribution to the tropical warming, reinforcing the mean SST intensification. Notably, the net LWF shows a pronounced positive trend in the equatorial region (Supplementary Fig. 11A). Surface heat flux anomalies are strongly modulated by atmospheric circulation

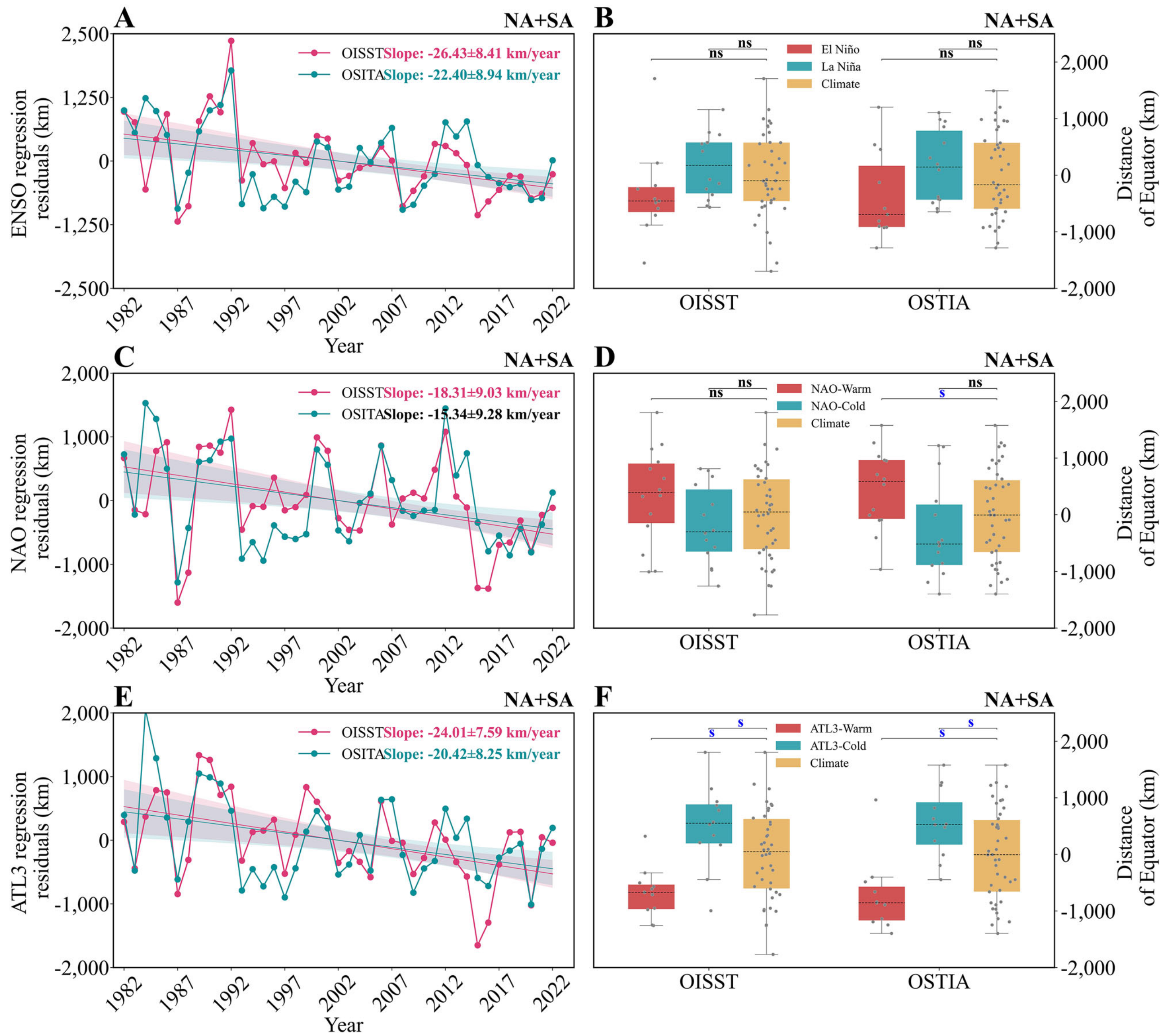

Fig. 3 | Role of interannual climate variabilities in impacting the equatorward shift of MHWC over the Atlantic basin during the period 1982–2022. A Residual temporal evolution of annual-mean MHWC latitude in the combined hemispheric domain after removing preceding winter El Niño-Southern Oscillation (ENSO) based on the OISST (red line) and OSTIA (green line) datasets. **C**, **E**: As (**A**), but for the results after removing preceding winter North Atlantic Oscillation (NAO) and concurrent Atlantic Niño (ATL3), respectively. **B** Composite of MHWC latitude anomalies during *El Niño* (red), *La Niña* (green), and climatological baseline (yellow). Black line indicates median composite anomalies. '*ns*' labels denote non-significant differences (Mann-Kendall test, $p = 0.1$). As in panel **B**, but for (**D**) NAO and (**F**) ATL3 phases: positive (red), negative (green), and climatological reference (yellow), respectively. Colored legends (**A**, **C**, **E**) denote trends significant at the 0.1 significance level, based on Mann-Kendall test analysis.

changes. Over the equatorial Atlantic, the weakening SLP trend (Supplementary Fig. 11C) fosters low-level convergence, thereby driving a significant increase in HCC (Supplementary Fig. 11B). This enhanced HCC formation is predominantly attributed to the intensification of convective high clouds (Supplementary Fig. 12), consistent with observed trends in deep convection[55]. Cloud changes exert opposing effects on radiation budgets. Increased cloudiness traps and re-emits net LWF, enhancing the downward longwave component (Supplementary Fig. 13). This reduces surface thermal loss and amplifies SST warming. Correlation analysis demonstrates negative relationships between the MHWC latitude and both tropical LWF (Fig. 4A) and HCC (Fig. 4B), which contrast with the positive correlations observed with SLP over tropics (Fig. 4C). These results indicate that the SST-SLP-HCC-LWF feedback facilitates enhanced warming and increased MHW occurrences in low-latitude regions, which is ultimately favorable for the MHWC equatorward shift.

To further evaluate the collective influence of multiple atmospheric drivers, a multiple linear regression (MLR) analysis was performed using regional mean net LWF, SLP, and cloud (averaged over 6°S-6°N) as predictors for the MHWC latitude. The results (Supplementary Fig. 14) provide evidence for the proposed atmospheric driving mechanism, with the MLR model accounting for a substantial 38.4% of the total variance in MHWC latitude. Within this framework, net LWF emerges as the predominant driver ($\beta = -0.70$, $p < 0.01$), underscoring its pivotal role in governing the observed equatorward shift.

To quantify this linkage, an interannual tropical LWF index was defined as the area-weighted average over 0°-6°N and 0°-6°S for the NA and SA, respectively. Significant negative correlations are observed between the areal-mean SLP series and MHWC latitude, with coefficients of -0.41 and -0.38 for the NA and SA, respectively, indicating that reduced LWF in the equatorial tropics is associated with an equatorward shift of MHWC

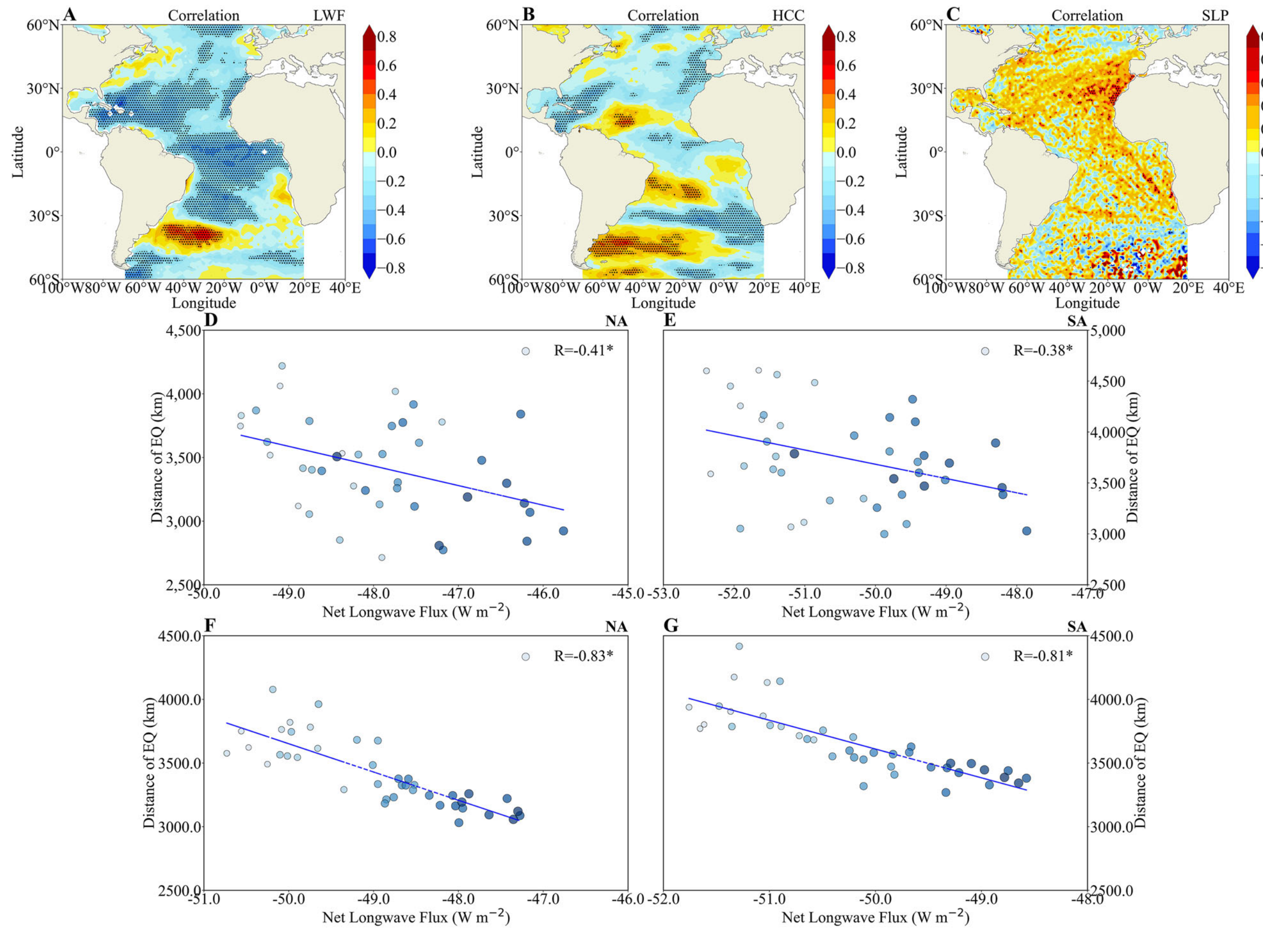

Fig. 4 | Physical processes for the equatorward shift of MHWC. A Spatial distributions of correlations between the annual-mean longwave radiation flux (LWF; positive downward, units: Wm^{-2}) from the European Centre for Medium-Range Weather Forecasts (ECMWF) Reanalysis v5 (ERA5) and the annual-mean latitude of MHWC during period 1982–2022. **B**, **C** As **A**, but for spatial correlation coefficients between MHWC latitude and total cloud cover (TCC) from the ERA5, and sea level pressure (SLP, units: hPa) from the International Comprehensive Ocean-Atmosphere Data Set (ICOADS), respectively. Black dots in (**A**–**C**) indicate trends significant at the 0.1 significance level, based on a two-sided Student's *t*-test. Scatterplot and linear fit of the LWF calculated from the ERA5 against the MHWC latitude in the NA (**D**) and SA (**E**); with correlation coefficients shown in the upper right corner, the asterisk indicates statistical significance at the 0.1 level. The diameter and color of the bubble represent the sequence of years, the larger and darker-colored bubbles indicate the later of the year. Considering the role of tropical LWF, the areal-mean LWF over 0°-6°N for the NA and 0°-6°S for the SA. **F**, **G** As in (**D**, **E**), but for the results from the ensemble mean of CMIP6 historical simulations. When selecting CMIP6 models, two primary criteria were considered: Consistency of simulation period with observation period (1982-2023). Availability of longwave radiation data for the same time period within the model outputs. Based on these comprehensive considerations, only 19 models (Supplementary Table 3) met both conditions. The ensemble mean field of these 19 models was then calculated and presented in (**F**) and (**G**).

(Fig. 4D, E). However, it is not the case for net shortwave radiation and total net heat flux, showing are statistically insignificant relationships with MHWC latitude (figure not shown). Consequently, the role of net shortwave radiation and total net heat flux in the migration of MHWC is not discussed. Further evidence supporting the role of LWF variation in MHWC migration comes from simulations of 19 CMIP6 models. Despite inter-model variability, all models consistently show a decreasing trend in net tropical LWF and significant negative correlations with modeled MHWC latitude (Supplementary Table 4). The multi-model ensemble mean also displays a significant negative correlation (Fig. 4F, G), further demonstrating that lower net LWF emission corresponds to a more equatorward shift of the MHWC. Collectively, these findings indicate that trends in tropical LWF likely constitute an important physical mechanism driving the observed equatorward shift of MHWC.

Additionally, we further examined the role of oceanic dynamics in facilitating the equatorward shift of MHWC. A zonal SLP gradient index ($\Delta SLP = SLP\_East - SLP\_West$) is defined as the difference in regional-averaged SLP between the eastern equatorial Atlantic (Box E: 15°W-5°E, 6°S-6°N) and the western equatorial Atlantic (Box W: 45°W-25°W, 6°S-6°N). It exhibits a significant weakening trend (Supplementary Fig. 15), reflecting a flattened pressure contrast across the equatorial Atlantic. This reduction in ΔSLP provides direct dynamical evidence for the relaxation of the easterly trade winds, a process that critically modulates the upper ocean heat budget. The observed wind relaxation triggers a sequence of dynamic feedbacks: first, it suppresses vertical mixing and offshore Ekman transport, thereby curtailing the upwelling of cold subsurface water in the tropical eastern Atlantic[57,58]. Second, it slows the horizontal advection of cooler water from higher latitudes. These changes effectively reduce the cooling power of the ocean, consistent with previous work[48]. This finding suggests that the oceanic dynamic feedback operates synergistically with the HCC-mediated longwave trapping, by concurrently reducing heat loss from both the atmosphere (longwave radiation) and the subsurface ocean (upwelling/mixing), together promoting the localized SST warming that anchors the equatorward shift of MHWC.

Therefore, the equatorward shift of the Atlantic MHWC is collectively driven by a synergy of thermodynamic feedback and adjusted ocean-atmosphere dynamics. Specifically, a positive feedback loop involving SST-SLP-HCC-LWF reduces surface heat loss. Simultaneously, the weakening zonal SLP gradient triggers a relaxation of the easterly trade winds, which subsequently suppresses vertical upwelling and horizontal advection. These

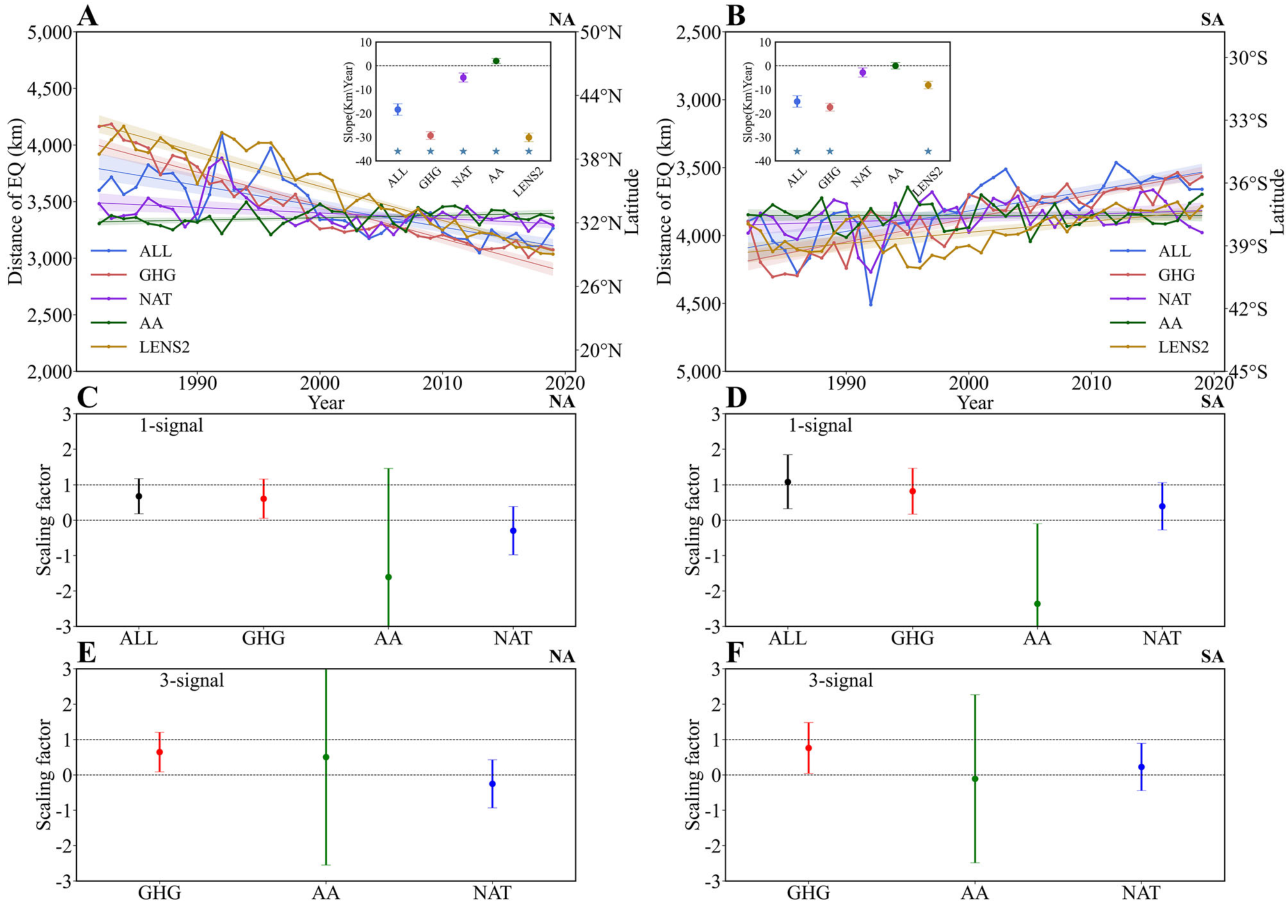

Fig. 5 | Anthropogenic forcing drives equatorward shift of Atlantic MHWC during period 1982–2019. A, B Linear trend of Atlantic MHWC under historical forcing: combined anthropogenic and natural forcing (ALL), greenhouse gas forcing (GHG), natural forcing (NAT), anthropogenic aerosol forcing (AA), and the CESM2 large ensemble (LENS2) for the NA (**A**) and SA (**B**). Shading denotes trends significant at the 0.1 level via a block-bootstrap resampling test (10,000 iterations). Insets: Hemispheric shift rates under representative scenarios, with blue pentagrams indicating statistically significant at the 0.1 level. Optimal fingerprinting detection-attribution results for NA (**C**, **E**) and SA (**D**, **F**). Single-signal scaling factors for NA (**C**) and SA (**D**). Three-signal scaling factors isolating GHG, AA, and NAT contributions for NA (**E**) and SA (**F**). Colored bars represent best estimates with 10th–90th percentile confidence intervals (CIs). Detection robustness requires CIs > 0; attribution validity demands inclusion of unity within CIs.

combined processes effectively facilitate equatorial heat accumulation, leading to the observed equatorward shift of the MHWC.

Detection and attribution analysis

Using multi-model ensembles from the CMIP6 and Community Earth System Model 2 large-ensemble simulations (LENS2), we evaluate the impacts of anthropogenic and nature forcing on the equatorward shift of MHWC. Four scenarios are used: historical forcing (ALL, combining anthropogenic and natural forcing), natural-only forcing (NAT), greenhouse gas-only forcing (GHG), and anthropogenic aerosol-only forcing (AA) (**CMIP6 products in Methods**, Supplementary Table 3).

Under both ALL and GHG forcing scenarios, the MHWC in both NA and SA exhibits a clear equatorward shift (Fig. 5A, B). The shift rate follows the order GHG > ALL, suggesting that the migration is primarily driven by greenhouse gas-induced warming, while AA exerts a partial counteractive effect. Specifically, while GHG promotes robust equatorward displacement, AA forcing induces an insignificant poleward shift, particularly in the NA, as aerosol-induced regional cooling partially offsets GHG-driven tropical warming[59]. Additionally, the systematic overestimation of shift rates in CMIP6 ALL forcing likely reflects systemic model biases in simulating MHW frequency (Supplementary Fig. 16) and SST trends (Supplementary Fig. 17) in tropical regions[5,60], which may be further exacerbated by the relatively low model resolution[29]. Indeed, simulations from LENS2 replicate this equatorward shift but amplify its magnitude, highlighting how assessment uncertainties are sensitive to model fidelity. Mechanistic analysis reveals that the tropical SST–SLP–HCC–LWF feedback, coupled with the weakening of equatorial and coastal upwelling in low-latitude regions, drives anomalous tropical warming. This synergy accelerates the increase in MHW frequency relative to higher latitudes, ultimately propelling the equatorward shift of the MHWC. Further comparison shows that the trend in tropical net LWF under GHG forcing significantly exceeds that in NAT forcing (Supplementary Fig. 18). This disparity indicates reduced net longwave heat loss and enhanced ocean heat gain under GHG-driven scenarios, providing an attribution-based physical link to the observed shift.

To quantify anthropogenic contributions, we further employ an optimal fingerprinting technique using generalized multivariate linear regression[61,62]. This method isolates spatiotemporal covariance patterns between observations and forced responses while accounting for internal variability (**Optimal Fingerprinting Detection and Attribution Method in Methods**). Through both single- and three-signal detection frameworks, scaling factors (β) with 90% confidence intervals (CIs) are derived for NA and SA basins. In all cases, the regression residuals satisfied consistency thresholds, confirming that the model-simulated internal variability is compatible with the observations. According to Detection and Attribution protocols, detection is achieved when the β is significantly greater than zero (the lower bound of the 90% CIs is above zero), while attribution is established when the CIs also encompass unity.

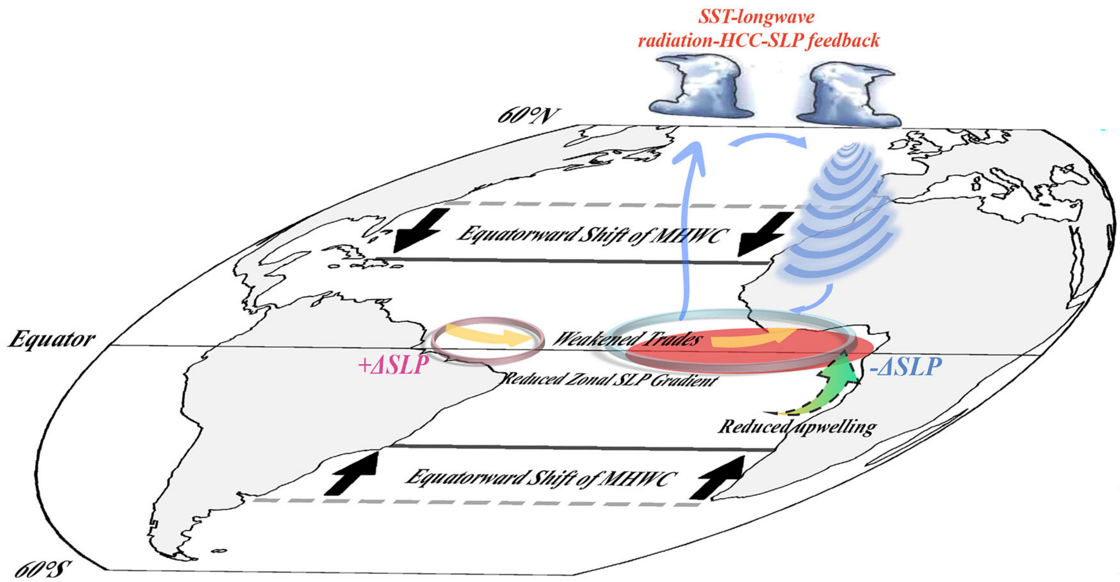

Fig. 6 | Schematic representation of the mechanisms driving the equatorward shift of the Atlantic MHWC. The dashed and solid black lines indicate the mean positions of the MHWC during the initial and final decades of the study period, respectively, with black arrows highlighting the pronounced equatorward migration. Equatorial positive SSTA are denoted by red shading. The intensified convection (upward-curving blue arrows), cloud icons, enhanced downward longwave radiation (downward-propagating wave patterns), and reduced SLP (blue circle) collectively illustrate the SSTA-LWF-HCC-SLP positive feedback mechanism. The blue and red circles represent centers of weakened and enhanced SLP over the equator region, respectively. This zonal SLP dipole signifies a reduction in the pressure gradient and a subsequent weakening of the trade winds, as illustrated by the yellow arrows. The green arrows with dashed lines represent the reduced vertical ocean mixing and weakened upwelling. Together, these processes demonstrate the synergy between radiation feedback and oceanic dynamic processes in facilitating the equatorward shift of MHWC.

Single-signal analysis detected significant ALL and GHG forcing impacts ($\beta > 0$) but found no discernible NAT or AA influences (Fig. 5C, D). To address potential covariance among external forcing, we conduct three-signal detection analysis to isolate distinct forcing contributions. This multi-factorial attribution framework definitively establishes that the observed equatorward shift of Atlantic MHWC predominantly originates from anthropogenic influences, wherein GHG forcing emerges as the principal driver (Fig. 5E, F). Similarly, an enhanced equatorial warming trend has been observed in the tropical Atlantic, which fingerprinting attribution analysis identifies as a clear signal of GHG forcing[48]. However, model simulations systematically overestimated GHG-induced shift rates in both NA and SA basins ($\beta < 1$). These overestimations are also present in the linear trends slope of the MHWC equatorward shift rates between the observations and simulations (Fig. 2A, C vs. Fig. 5A, B).

Therefore, these findings align with identified physical drivers, particularly SST-SLP-cloud-longwave interactions and oceanic dynamics changes over the tropical regions. The convergence of dynamical mechanisms and detection-attribution evidence establishes that anthropogenic GHG emissions amplify thermal atmosphere-ocean coupling[63], constituting primary thermodynamic drivers of equatorward shift of Atlantic MHWC.

Discussion

Observational records and climate model outputs demonstrate significant intensification in Atlantic MHW frequency under global warming[26,34]. Nevertheless, Atlantic SST warming manifests pronounced meridional asymmetry, with extra-tropical regions warming faster than tropical zones[64]. How these latitudinally divergent thermal forcing modulate marine extremes, like MHW frequency distributions, remains unresolved. In this study, we demonstrate that Atlantic MHWC has migrated equatorward over the past four decades, with an average rate of approximately 1° latitude per decade observed in both northern and southern basins. This equatorward shift suggests that MHW frequency escalates disproportionately in climatologically warm ocean regions, amplifying MHW frequency and extreme event probabilities in tropical basins, consistent with the 'warm getting warmer' situation reported in the land heatwave configuration[65]. Additionally, mid-latitude oceanic marine heatwave frequency has also shown a significant increasing trend over the past few decades, especially in WBC regions. However, its rate of increase is relatively lower compared to tropical regions. Therefore, such tropical intensification imposes critical ecological stressors on thermally sensitive ecosystems, including coral reefs' bleaching risk[2–4,6] and fisheries production[8,9].

Significant positive trends in net surface heat flux are detected over the equatorial Atlantic, providing a robust thermodynamic environment for SST warming. Our findings reveal that the SST-SLP-cloud-longwave feedback, where warming reinforces convective cloudiness to trap longwave radiation, systematically promotes equatorial Atlantic warming and serves as the primary driver for the observed equatorward MHWC shift. While the shortwave radiation-SST feedback also influences SSTA through cloud-albedo modulation[44,46,47], our analysis indicates that its contribution to the specific equatorward shift of the MHWC is less deterministic than the longwave component. Beyond these radiative factors, oceanic dynamical processes play a complementary and pivotal role in anchoring the MHWC shift. The observed weakening of the zonal SLP gradient across the Atlantic basin reflects a relaxation of equatorial easterly winds, which is intrinsically linked to the suppression of equatorial upwelling, a process that represents the primary oceanic dynamical mechanism driving anomalous warming in the tropical Atlantic[48]. These combined effects of reduced evaporative cooling and diminished wind-driven ocean ventilation create a physically consistent heat trap in the upper ocean (Fig. 6). Collectively, our results indicate that the equatorward shift of the MHWC is a complex manifestation of enhanced longwave-SST feedback acting in synergy with weakened oceanic cooling mechanisms, both of which represent a robust forced response to a warming climate.

Additionally, high MHW frequencies are notably observed in mid-latitude Western Boundary Current (WBC) regions, specifically the Gulf Stream (GS) and Brazil Current (BRZ) areas (Fig. 1). Analysis of eddy kinetic energy (EKE, **Eddy Kinetic Energy in Methods**) derived from Archiving, Validation and Interpretation of Satellite Oceanographic (AVISO) dataset reveals a pronounced intensification in these eddy-rich zones, contrasting with the reduced variability in the tropics (Supplementary Fig. 19). This spatial coherence suggests that strengthened mesoscale activity is a primary driver of MHW dynamics and accelerated warming in the Atlantic's western boundary extensions, consistent with the critical role of eddies in governing MHW characteristics[36]. For instance, the 2015/2016 Tasman Sea MHWs event coincided with anomalous southward flow and intensified EKE associated with enhanced southward extension of the East Australian Current[40]. However, in the Atlantic, eddy influences display marked spatial heterogeneity, predominantly governing MHW dynamics in Western Boundary Currents and their extensions. Additionally, it is reported that zonal displacement patterns of MHW further exhibit spatiotemporal coherence with mesoscale eddy distributions, where high-intensity MHW regions align closely with EKE maxima[66]. Such coherence suggests eddies act as dynamic puppeteers governing both the timing and spatial propagation of MHW. Therefore, the future impact of the latitudinal tug-of-war between large-scale equatorial warming (driven by cloud-radiative feedback) and eddy-driven heat transport on the formation of Atlantic MHWs in WBC regions warrants further investigation. Additionally, while our study bridges mesoscale dynamics with basin-scale thermodynamics, unresolved vertical eddy processes, particularly their modulation of mixed-layer heat budgets, represent critical knowledge gaps for predicting MHWs responses to amplified climate variability[33,36]. These interactions highlight the inadequacy of single-scale frameworks in projecting marine heat extremes under anthropogenic forcing.

A key finding of this study is the robust equatorward migration of MHWC after adjusting for linear climate signals. However, interannual variability may exert complex nonlinear impacts on this shift. The relationship between climate variabilities and the tropical Atlantic energy budget may be state-dependent. The efficiency of the identified cloud-longwave radiation feedback could be nonlinearly modulated by the background SST state or the depth of the thermocline[55,67–69], leading to accelerated periods in MHWC migration during certain climate phases. Additionally, nonlinear compound effects, where the simultaneous occurrence of multiple climate modes produces a shift greater than the sum of their individual impacts, could account for some of the extreme latitudinal anomalies observed in the record. Future studies utilizing nonlinear dynamical frameworks are required to further disentangle these interactions and better quantify the sensitivity of MHWC spatial patterns to a warming climate.

Additionally, simulations demonstrate that anthropogenic GHG forcing is the dominant driver of the observed equatorward shift of Atlantic MHWC, while AA partially offset this displacement regionally[59,70]. The hierarchical forcing hierarchy (GHG > ALL > observations) and the contrasting roles of GHG and AA forcing highlight the complex interplay between thermodynamic and regional-scale feedback under anthropogenic climate change. The systematic overestimation of GHG-induced shift rates in models underscores unresolved challenges in representing tropical SST trends and atmosphere-ocean coupling processes. These biases may arise from inadequate resolution of mesoscale eddy dynamics or misrepresentation of cloud-SST feedback[5,60,71], which are critical for modulating thermal gradients and atmospheric circulation patterns. Furthermore, under the high-emission SSP5-8.5 scenario, the equatorward shift of the Atlantic MHWC in both NA and SA basins is projected to accelerate during 2020-2050 (Supplementary Fig. 20), providing further evidence for the dominant role of anthropogenic GHG forcing. While our use of a contemporary baseline (2020-2049) maintains the statistical sensitivity of the MHW frequency metric for the analyzed period, we acknowledge that in even more extreme or longer-term warming scenarios, the frequency-weighted centroid may be prone to saturation as events become increasingly persistent. In such cases, alternative metrics such as total MHW days or cumulative intensity-weighted centroids could provide complementary insights into the spatial redistribution of marine thermal extremes.

This study advances the mechanistic understanding of MHWC migrates by integrating detection-attribution evidence with dynamical diagnostics. Given its more complex circulation system and climate variability, understanding the specific implications of the MHWC shift in the Pacific Ocean is particularly crucial and warrants further investigation. Such refinements will enhance predictive capacity for marine ecosystem responses[3,9] and weather pattern shifts[16,17] in a climate regime increasingly characterized by frequent MHWs under anthropogenic influence.

Methods

Observational products

Two observational sea surface temperature (SST) datasets are utilized to analyze the marine heatwaves (MHWs) frequency and their latitudinal position. The National Oceanic and Atmospheric Administration (NOAA) Optimum Interpolation Sea Surface Temperature Version 2.0 (OISST), features a horizontal resolution of 0.25° × 0.25°[72]. The Operational Sea Surface Temperature and Ice Analysis (OSTIA), integrates satellite and in situ observations to generate high-resolution SST analyses and intercomparison products for the global ocean. OSTIA products include foundation SST (the SST from which the diurnal cycle develops), hourly skin SST, and the Group for High-Resolution SST Multi-Product Ensemble with a spatial resolution of 1/20° × 1/20°[73]. Both datasets provide daily temporal resolution, spanning the period from January 1, 1982, to December 31, 2023. To ensure data standardization and consistency, the two observational datasets, OISST (0.25° × 0.25°) and OSTIA (1/20° × 1/20°), are harmonized into a common resolution of 0.25° × 0.25°. Specifically, OSTIA data are interpolated into the OISST spatial grid using a bilinear scheme. This harmonized resolution is subsequently employed for the observational analysis of MHW frequency and movement trends.

Additionally, spatial trends in cloud cover, shortwave radiation flux, latent heat flux, sensible heat flux, and longwave radiation flux are analyzed using monthly-mean reanalysis data from the European Centre for Medium-Range Weather Forecasts (ECMWF) Reanalysis v5 (ERA5)[74] from 1982 to 2023. Additionally, the mean sea level pressure is derived from the International Comprehensive Ocean-Atmosphere Data Set (ICOADS) dataset from 1982 to 2023. The sea surface height derived from the Simple Ocean Data Assimilation (SODA) version 3.15.2[75,76] with horizontal resolution of 0.5° × 0.5° is used to calculate the geostrophic velocities from 1982 to 2023. Moreover, the eddy kinetic energy (EKE) dataset with horizontal resolution of 0.25° × 0.25° from Archiving, Validation and Interpretation of Satellite Oceanographic (AVISO) from 1993 to 2023 is utilized to explain the impacts of mesoscale eddies in the western boundary area on the higher frequency of MHWs over these regions.

While potential biases in longwave heat flux products have been noted[77], our interpretation relies on relative changes and trends rather than absolute magnitudes. These trend-based indices remain robust indicators of the underlying physical mechanisms, even in the presence of systematic offsets. Furthermore, to cross-validate our findings, we incorporated longwave heat flux data from the National Centers for Environmental Prediction Reanalysis (NCEP1) dataset (1982–2023). The remarkable consistency in trends observed between ERA5 (Supplementary Fig. 13) and NCEP1 (Supplementary Fig. 21) demonstrates the structural reliability of the proposed cloud–longwave feedback mechanism.

CMIP6 products

To examine the anthropogenic influence on the MHW centroids (MHWC) latitude shift, daily SST outputs from multi-model simulations driven by different external forcing from the Coupled Model Intercomparison Project Phase 6 (CMIP6)[78] are employed (Supplementary Table 3). Both combined and individual forcing are considered, including all external forcing (ALL, encompassing anthropogenic and natural forcing), greenhouse gas forcing alone (GHG), natural forcing alone (NAT), and anthropogenic aerosol forcing alone (AA). A total of 32 models with the first ensemble member (r1i1p1f1) are used for ALL forcing analysis. For ALL forcing simulations, 20 of the 32 models are extended to 2020 using SSP2-4.5 projections, while the remaining 12 models end in 2014. For GHG, NAT, and AA, 7 models with all available realizations are included, providing 32, 34, and 36 realizations, respectively, with data spanning from 1982 to 2020 (Supplementary

Table 5). In addition, 11 CMIP6 models from 2020 to 2050 under the high-emission SSP5-8.5 scenario are utilized for future projections (Supplementary Table 3). Additionally, 5 models from piControl simulations (r1i1p1f1) are utilized to estimate internal variability, comprising a total of 2800 model years (Supplementary Table 6). Furthermore, monthly surface downwelling and upwelling longwave radiation data, derived from 19 CMIP6 models (r1i1p1f1 realization under ALL external forcing, Supplementary Table 4), 6 models (r1i1p1f1 realization under NAT and GHG external forcing, Supplementary Table 7), and 14 models under CMIP6 SSP5-8.5 scenario (Supplementary Table 8) are used to corroborate the role of tropical ocean-atmosphere positive feedback in the equatorward displacement of the Atlantic MHWC.

To further assess the roles of internal variability and external forcing, daily SST outputs from the National Center for Atmospheric Research (NCAR) Community Earth System Model Version 2.0 (CESM2) Large Ensemble Project (LEN2) are analyzed[79,80]. This ensemble consists of 90 initial condition simulations, with historical simulations covering 1982-2014 and future projections under the SSP370 scenario for 2015–2020. Given that the 90 simulations from LENS2 share identical external forcing but differ in initial conditions, the ensemble mean is used to estimate the response to external forcing. For each model, daily SST data are interpolated into a common 2° × 2° resolution to calculate MHW frequency. For GHG, NAT, and AA, the multi-model ensemble mean is derived by computing the multi-realization mean within each model, followed by averaging across models to ensure equal weighting.

To evaluate the sensitivity of the MHWC shifts to the horizontal resolution, we further re-gridded the observational datasets to the same coarse grid. The results confirm that the observed equatorward shift of the MHWC remains consistent even at this lower resolution (Supplementary Fig. 22), suggesting that the 2° × 2° grid is sufficient to capture the key dynamics without biasing our mechanistic analysis. Furthermore, the monthly longwave flux data from the 19 models under CMIP6 ALL experiments, 6 models under CMIP6 NAT and GHG experiment, and 14 models under CMIP6 SSP5-8.5 scenario, are also interpolated to the corresponding 2° × 2° resolution consistency.

Climate indices

Interannual climate variability was removed from the annual-mean MHWC latitude time series by regressing the individual series from the northern Atlantic (NA) and southern Atlantic (SA) onto the climate indices and analyzing the residuals. Three principal climate indices representing dominant modes of variability: (1) Oceanic Niño Index (ONI) derived from the NOAA Climate Prediction Center (CPC), a measure of equatorial central Pacific SSTA indicative of the state of ENSO, is calculated as the areal-averaged SST anomalies (170°–120°W and 5°S–5°N). (2) North Atlantic Oscillation (NAO) index-consists of a north-south dipole in atmospheric pressure anomalies, with one center located over Greenland and the other center of opposite sign spanning the central latitudes of the North Atlantic between 35°N and 40°N. The index we used, derived from the NOAA CPC, is based on a rotated principal component analysis of monthly standardized 500-mb height anomalies in the North Atlantic poleward of 20°N[81]. (3) Atlantic Niño index (ATL3) is calculated as the areal-averaged SST anomalies in the region of 20°W-0°, 3°S-3°N[82] using the Hadley Centre Global Sea Ice and Sea Surface Temperature (HadISST) dataset.

To evaluate the influence of ENSO and ATL3 on the shift trends of MHWC, we utilize the preceding winter signals of these climatic indices (December^{-1}, January^{0}, February^{0}). Specifically, the MHWC latitude shift is assessed after removing the two climate indices averaged over these three months (Fig. 3A, C). For NAO, the analysis focused on removing the annual mean SSTA for the corresponding period, thereby obtaining the adjusted shift characteristics (Fig. 3E). Assuming a linear relationship between MHWC latitude and the three climate indices (ENSO, ATL3, and NAO), we first applied ordinary least squares (OLS) to fit this linear model. The influence of these climate signals was then removed by subtracting the fitted values from the original data. Finally, we quantified the secular trend using the resulting residuals, representing the dynamically adjusted MHWC anomalies. The residuals isolate the anthropogenically forced component of MHWC changes independent of dominant climate modes. While linear detrending via climate indices (ENSO, ATL3, NAO) provides first-order adjustment of interannual variability, this approach carries dual limitations: (1) climate indices incompletely represent climate mode spatial-temporal heterogeneity (e.g., ENSO diversity neglected in Niño 3.4)[83,84], and (2) linear stationarity assumptions fail to capture the nonstationary impacts (e.g., abrupt change) of climate modes[28]. Therefore, residual collinearity may still conflate forced responses and internal variability.

Furthermore, composite analysis is employed to investigate the impacts of climate variability on the meridional shift of MHWC. We examine the variations in MHWC latitude under positive and negative phases of the three climatic modes (Fig. 3B, D, F). For ENSO events, warm (cold) phases are identified as periods with SSTA exceeding (falling below) +0.5°C (−0.5°C) for at least five consecutive months. For NAO and ATL3, positive and negative events are identified using a threshold of ±0.5 standard deviations.

Definition of MHWs

In this study, MHWs are identified from daily SST time series, and their frequency, intensity, and duration are characterized through the calculation of relevant metrics. MHWs are defined as discrete, prolonged anomalously warm water events[1]. Specifically, "discrete" is quantitatively defined as an identifiable event with distinct start and end dates, "prolonged" refers to a minimum duration of 5 days, and "anomalously warm" is determined by referencing a seasonally varying baseline threshold. The identification of MHW events involve detecting periods where daily temperatures exceed the seasonally varying 90th percentile threshold for at least five consecutive days. Events separated by fewer than 2 days are considered a single event.

The definition of MHWs within the historical stage (1982 to 2023) is adapted as follows: for each grid point, SSTA are calculated by removing a climatology from 1983–2012, which serves as the basis for subsequent analysis. The 90th percentile threshold is computed by calculating daily SSTA within an 11–day window centered on each calendar day across all years of the climatological period, followed by smoothing using a 31–day moving average for each Julian day. The selection of an 11-day window and a 31-day moving average aims to ensure sufficient sample size for percentile estimation and to generate a smoothed climatological baseline[1]. The seasonally varying threshold enables the identification of anomalously warm events at any time of the year, rather than being limited to the warmest months. Each MHW event is characterized by a set of properties, including duration and multiple intensity metrics.

To evaluate the sensitivity of MHWs identification to the choice of threshold and climatological period, four additional comparative experiments are conducted (Supplementary Table 2). The results demonstrated that the statistical significance of the trends presented in the main text is insensitive to the percentile threshold (95th percentiles), the choice of climatological period (e.g., 1982–2023), and the inclusion or exclusion of the seasonal cycle (Supplementary Figs. 5, 6). Therefore, the conclusions regarding the latitude of MHWC changes exhibit robust reliability.

For the future projections under the SSP5-8.5 scenario (2020 to 2050), MHWs are defined using a contemporary climatological baseline based on the period 2020–2049. By employing this moving baseline, the MHW frequency remains a statistically sensitive metric that captures discrete extreme events relative to the projected warming state. This approach prevents the 'saturation' of MHW frequency that could occur if a historical baseline were used, where the ocean state might shift toward a single, near-permanent heatwave event under intense global warming.

Definition of MHWC

To assess the shift trends of MHWC in the Atlantic, we calculate the annual-mean MHWC latitude using the following formula after determining the

MHW frequency:

$$\bar{\varphi}(i) = \frac{\sum_{m=1}^{M(i)} |\varphi(i,m)| \cdot N(i,m)}{\sum_{m=1}^{M(i)} N(i,m)} \quad (1)$$

where $\bar{\varphi}(i)$ is the MHWC latitude for year (i). $|\varphi(i,m)|$ denotes the absolute value of the latitude of MHW events at grid cell (m) during year (i). $N(i,m)$ represents the total number of MHW events at grid cell (m) during year (i), and $M(i)$ is the total grid number of MHW events during year (i). This variable ($\bar{\varphi}(i)$) quantifies the average latitude of MHWs occurrences within a given year. We perform a trend analysis on these annual-mean MHW locations. A negative trend slope indicates an equatorward shift of the Atlantic MHWC, implying a higher frequency of MHW events in lower latitudes compared to higher latitudes. Conversely, a positive trend slope suggests a poleward shift in MHWC.

Annual and seasonal definitions for the Atlantic

To align with the seasonal cycles of both NA and SA regions, this study defines a year as the period from March of the current year to February of the following year. This approach prevents the artificial splitting of the December–February (DJF) season, which represents the austral summer and boreal winter across two consecutive calendar years. By doing so, we ensure that a complete seasonal cycle of ocean warming and cooling is captured as a single, continuous occurrence within each statistical year. Consequently, for observational data, the study period spans from 1982 to 2022. For CMIP6 data, the study period extends from 1982 to 2019. Seasons are defined as follows: March to May as MAM, June to August as JJA, September to November as SON, and December to February of the following year as DJF.

Optimal fingerprinting detection and attribution method

The detection of climate change involves confirming the occurrence of a change at a specific statistical confidence level, without addressing its underlying causes. For detected changes, attribution refers to the estimation, at a given confidence level, of the relative contributions of multiple factors to the observed change[61,62].

In this paper, in order to detect anthropogenic influence rigorously, we use an optimal fingerprinting method based on a generalized multivariate linear regression of the observed or reconstructed magnitude of the MHWC as a combination of climate responses to external plus internal forcing[61]. To detect and attribute the changes in the magnitude of the observed MHWC to different external forcing (that is, GHG, AA, NAT), we regress the observed latitude of the MHWC onto different external forcing under one- and three-signal settings, respectively. The specific regression setting for the detection and attribution analysis is as follows:

$$y = \sum_{i=1}^{m} \beta_i x_i + \varepsilon_0 \quad (2)$$

where y represents the ensemble mean of MHWC latitude derived from multiple observational datasets. x_i denotes the model-simulated temporal responses to the i-th external forcing factor based on the ensemble mean of model simulations. m indicates the number of external forcing (in this study, GHG, AA, and NAT). ε_0 represents the observational noise associated with internal variability, and β_i are the scaling factors that quantify the contribution of each external forcing to the observed changes. Additionally, the OLS method was employed to estimate the response coefficients β. This method minimizes the sum of squared residuals between the observed values and the model-predicted values, thereby quantifying the contributions of external forcing factors to the observed climate changes. Detection analysis requires reducing both the temporal and spatial dimensions[61,85]. Therefore, to remove interannual variability signals, a 10-year moving average is applied to observed MHWC latitude and simulated MHWC latitude under different external forcing.

An external forcing signal is considered detectable in the observations if its scaling factor (β) is significantly greater than zero (i.e., the lower bound of the 90% confidence interval (CI) is above zero). Furthermore, the observed changes are attributed to a specific forcing if its scaling factor is significantly greater than zero and its 90% CI encompasses unity, while the influences of other forcing can be excluded (i.e., their β values are either not significantly greater than zero or their 90% CIs do not include 1)[86]. A scaling factor β greater (smaller) than 1 indicates that the ensemble simulations underestimate (overestimate) the magnitude of the observed response[87].

In this study, a temporal discrepancy exists between the observational and model data: the observational data span the period from 1982 to 2022, while the model data cover 1982 to 2019. To calculate the optimal fingerprint scaling factors, annual mean data from 1982 to 2019 are used for both observations and model simulations. We use output from six climate models across three experimental groups, comprising 102 ensemble members: 32 members from GHG forcing experiments, 34 members from AA forcing experiments, and 36 members from NAT forcing experiments (Supplementary Table 5). For historical ALL forcing simulations, we employ data from the r1i1p1f1 experiment variant spanning 1982-2020, totaling 20 simulations (Supplementary Table 4). To evaluate internal variability, this study utilizes modeled data from the 1850 control experiments of five models (Supplementary Table 6), resulting in a total of 2800 years of control experiment data. These data are divided into 80 noise segments, each matching the length of the observational record. The total of 80 noise segments is then equally partitioned into two independent groups: one group is used for optimal estimation, while the other is employed for residual consistency testing[61], which assesses whether the simulated internal variability in the models aligns with the observed variability.

In the detection analyses, we first apply a one-signal analysis to detect the effects of individual forcing, by regressing the observed values onto the simulated values under ALL, GHG, NAT, and AA forcing, one at a time. Considering correlations between signals, we then apply three-signal analyses to distinguish the influence of one forcing from the others.

Eddy kinetic energy

The eddy kinetic energy (EKE) is derived from geostrophic velocity anomalies, specifically the zonal (U'_g) and meridional (V'_g) components[88], using the following equation:

$$EKE = \frac{1}{2} \times \left({U'_g}^2 + {V'_g}^2 \right), \quad (3)$$

Here, U'_g and V'_g represent the fluctuating components of the zonal and meridional geostrophic velocities, respectively, and are calculated as:

$$U'_g = -\frac{g}{f}\frac{\partial \eta}{\partial y}, \quad (4)$$

$$V'_g = \frac{g}{f}\frac{\partial \eta}{\partial x}, \quad (5)$$

where η denotes sea level anomalies, g is the acceleration due to gravity, f is the Coriolis parameter, and ∂x and ∂y represent the distances in the eastward and northward directions, respectively. The EKE (Supplementary Fig. 19) calculated using the sea level height dataset from SODA spanning 1982 to 2023 shows a similar increasing trend with the observed feature in the western boundary area (Supplementary Fig. 23), which indicates the spatial distribution of EKE trends exhibits minimal sensitivity to temporal coverage, indicating robust statistical linkages across varying time window selections.

Data availability

The data for atmosphere used in the manuscript are publicly available for OISST (https://www.ncei.noaa.gov/products/optimum-interpolation-sst), OSITA(https://data.marine.copernicus.eu/product/SST_GLO_SST_L4_

NRT_OBSERVATIONS_010_001/services), CMIP6 modeled data (https://aims2.llnl.gov/search/cmip6/), CESM2 large ensemble dataset (https://www.earthsystemgrid.org/dataset/ucar.cgd.cesm2le.ocn.proc.daily_ave.html), ERA5 (https://www.ecmwf.int/en/forecasts/dataset/ecmwf-reanalysis-v5), ONI index (https://www.cpc.ncep.noaa.gov/products/analysis_monitoring/ensostuff/ONI_v5.php), NAO index (https://psl.noaa.gov/data/climateindices/list/), HadISST dataset (https://www.metoffice.gov.uk/hadobs/hadisst/data/download.html), AVISO dataset (https://www.aviso.altimetry.fr/en/data/data-access.html), SODA dataset (http://dsrs.atmos.umd.edu/DATA/soda3.15.2/REGRIDED/ocean/), ICOADS dataset (https://www.ncei.noaa.gov/products/international-comprehensive-ocean-atmosphere-data-set), and NCEP1 dataset (https://psl.noaa.gov/data/gridded/data.ncep.reanalysis.html).

Code availability

Any codes used in the manuscript are available upon request from jixl@nmefc.cn.

Received: 11 January 2026; Accepted: 27 April 2026;
Published online: 07 May 2026

References

1. Hobday, A. J. et al. A hierarchical approach to defining marine heatwaves. *Prog. Oceanogr.* **141**, 227–238, https://doi.org/10.1016/j.pocean.2015.12.014 (2016).
2. Hughes, T. P. et al. Global warming transforms coral reef assemblages. *Nature* **556**, 492–496, https://doi.org/10.1038/s41586-018-0041-2 (2018).
3. Eakin, C. M., Sweatman, H. P. A. & Brainard, R. E. The 2014–2017 global-scale coral bleaching event: insights and impacts. *Coral Reefs* **38**, 539–545, https://doi.org/10.1007/s00338-019-01844-2 (2019).
4. Lough, J. M., Anderson, K. D. & Hughes, T. P. Increasing thermal stress for tropical coral reefs: 1871–2017. *Sci. Rep.* **8**, https://doi.org/10.1038/s41598-018-24530-9 (2018).
5. Li, X. & Donner, S. Assessing future projections of warm-season marine heatwave characteristics with three CMIP6 models. *J. Geophys. Res.: Oceans* **128**, https://doi.org/10.1029/2022jc019253 (2023).
6. Rodrigues, R. R., Gonçalves Neto, A. H., Vieira, E. A. & Longo, G. O. The severe 2020 coral bleaching event in the tropical Atlantic linked to marine heatwaves. *Commun. Earth Environ.* **6**, https://doi.org/10.1038/s43247-025-02195-3 (2025).
7. Smale, D. A. et al. Marine heatwaves threaten global biodiversity and the provision of ecosystem services. *Nat. Clim. Change* **9**, 306–312, https://doi.org/10.1038/s41558-019-0412-1 (2019).
8. Free, C. M. et al. Impacts of historical warming on marine fisheries production. *Science* **363**, 979–983, https://doi.org/10.1126/science.aau1758 (2019).
9. Cheung, W. W. L. & Frölicher, T. L. Marine heatwaves exacerbate climate change impacts for fisheries in the northeast Pacific. *Sci. Rep.* **10**, https://doi.org/10.1038/s41598-020-63650-z (2020).
10. Capotondi, A. et al. A global overview of marine heatwaves in a changing climate. *Commun. Earth Environ.* **5**, (2024).
11. Wernberg, T. et al. Climate-driven regime shift of a temperate marine ecosystem. *Science* **353**, 169–172, https://doi.org/10.1126/science.aad8745 (2016).
12. Arafeh-Dalmau, N. et al. Extreme Marine Heatwaves Alter Kelp Forest Community Near Its Equatorward Distribution Limit. *Front. Mar. Sci.* **6**, https://doi.org/10.3389/fmars.2019.00499 (2019).
13. Kossin, J. P. Hurricane intensification along United States coast suppressed during active hurricane periods. *Nature* **541**, 390–393, https://doi.org/10.1038/nature20783 (2017).
14. Balaguru, K., Foltz, G. R. & Leung, L. R. Increasing Magnitude of Hurricane Rapid Intensification in the Central and Eastern Tropical Atlantic. *Geophys. Res. Lett.* **45**, 4238–4247, https://doi.org/10.1029/2018gl077597 (2018).
15. Kossin, J. P. A global slowdown of tropical-cyclone translation speed. *Nature* **558**, 104–107, https://doi.org/10.1038/s41586-018-0158-3 (2018).
16. Duchez, A. et al. Drivers of exceptionally cold North Atlantic Ocean temperatures and their link to the 2015 European heat wave. *Environ. Res. Lett.* **11**, https://doi.org/10.1088/1748-9326/11/7/074004 (2016).
17. Shi, H. et al. Co-occurrence of California Drought and Northeast Pacific Marine heatwaves under climate change. *Geophys. Res. Lett.* **48**, https://doi.org/10.1029/2021gl092765 (2021).
18. Scannell, H. A., Pershing, A. J., Alexander, M. A., Thomas, A. C. & Mills, K. E. Frequency of marine heatwaves in the North Atlantic and North Pacific since 1950. *Geophys. Res. Lett.* **43**, 2069–2076, https://doi.org/10.1002/2015gl067308 (2016).
19. Rodrigues, R. R., Taschetto, A. S., Sen Gupta, A. & Foltz, G. R. Common cause for severe droughts in South America and marine heatwaves in the South Atlantic. *Nat. Geosci.* **12**, 620–626, https://doi.org/10.1038/s41561-019-0393-8 (2019).
20. Manta, G., de Mello, S., Trinchin, R., Badagian, J. & Barreiro, M. The 2017 Record Marine Heatwave in the Southwestern Atlantic Shelf. *Geophys. Res. Lett.* **45**, https://doi.org/10.1029/2018gl081070 (2018).
21. Oliver, E. C. J. et al. Marine heatwaves. *Annu. Rev. Mar. Sci.* **13**, 313–342, https://doi.org/10.1146/annurev-marine-032720-095144 (2021).
22. Plecha, S. M., Soares, P. M. M., Silva-Fernandes, S. M. & Cabos, W. On the uncertainty of future projections of Marine Heatwave events in the North Atlantic Ocean. *Clim. Dyn.* **56**, 2027–2056, https://doi.org/10.1007/s00382-020-05529-3 (2021).
23. Frölicher, T. L., Fischer, E. M. & Gruber, N. Marine heatwaves under global warming. *Nature* **560**, 360–364, https://doi.org/10.1038/s41586-018-0383-9 (2018).
24. Oliver, E. C. J. et al. Projected marine heatwaves in the 21st Century and the potential for ecological impact. *Front. Mar. Sci.* **6**, https://doi.org/10.3389/fmars.2019.00734 (2019).
25. Collins, M., Sutherland, L., Bouwer, L., Cheong, S.-M. & Frölicher, T. in *IPCC Special Report on the Ocean and Cryosphere in a Changing Climate* Ch. Chapter 6, 589-656 (2019).
26. Holbrook, N. J. et al. in *El Niño Southern Oscillation in a Changing Climate* Vol. 18 *Geophysical Monograph Series* (eds M. J. McPhaden, A Santoso, & W Cai) 409–428 (John Wiley & Sons, Inc., 2020).
27. Ren, X., Liu, W., Capotondi, A., Amaya, D. J. & Holbrook, N. J. The Pacific Decadal Oscillation modulated marine heatwaves in the Northeast Pacific during past decades. *Commun. Earth Environ.* **4**, https://doi.org/10.1038/s43247-023-00863-w (2023).
28. Wei, J., Han, W., Wang, W., Zhang, L. & Rajagopalan, B. Intensification of heatwaves in China in recent decades: Roles of climate modes. *npj Clim. Atmos. Sci.* **6**, https://doi.org/10.1038/s41612-023-00428-w (2023).
29. Dong, L. et al. Roles of external forcing and internal variability in global marine heatwaves change during 1982–2021. *Geophys. Res. Lett.* **51**, https://doi.org/10.1029/2023gl107557 (2024).
30. Dong, M. et al. PDO modulates co-occurring summertime marine heatwaves in the extratropical North Pacific and Atlantic. *J. Geophys. Res.: Atmos.* **130**, https://doi.org/10.1029/2024jd042143 (2025).
31. Vogt, L., Burger, F. A., Griffies, S. M. & Frölicher, T. L. Local drivers of marine heatwaves: a global analysis with an Earth System Model. *Front. Clim.* **4**, https://doi.org/10.3389/fclim.2022.847995 (2022).
32. Frajka-Williams, E. et al. Atlantic Meridional overturning circulation: observed transport and variability. *Front. Mar. Sci.* **6**, https://doi.org/10.3389/fmars.2019.00260 (2019).
33. Holbrook, N. J. et al. A global assessment of marine heatwaves and their drivers. *Nat. Commun.* **10**, https://doi.org/10.1038/s41467-019-10206-z (2019).

34. Sen Gupta, A. et al. Drivers and impacts of the most extreme marine heatwave events. *Sci. Rep.* **10**, https://doi.org/10.1038/s41598-020-75445-3 (2020).
35. Kajtar, J. B., Bachman, S. D., Holbrook, N. J. & Pilo, G. S. Drivers, Dynamics, and persistence of the 2017/2018 Tasman Sea Marine Heatwave. *J. Geophys. Res.: Oceans* **127**, https://doi.org/10.1029/2022jc018931 (2022).
36. Bian, C. et al. Oceanic mesoscale eddies as crucial drivers of global marine heatwaves. *Nat. Commun.* **14**, https://doi.org/10.1038/s41467-023-38811-z (2023).
37. Elzahaby, Y. & Schaeffer, A. Observational insight into the subsurface anomalies of marine heatwaves. *Front. Mar. Sci.* **6**, https://doi.org/10.3389/fmars.2019.00745 (2019).
38. Myers, T. A., Mechoso, C. R., Cesana, G. V., DeFlorio, M. J. & Waliser, D. E. Cloud feedback key to marine heatwave off Baja California. *Geophys. Res. Lett.* **45**, 4345–4352, https://doi.org/10.1029/2018gl078242 (2018).
39. Schmeisser, L., Bond, N. A., Siedlecki, S. A. & Ackerman, T. P. The role of Clouds and surface heat fluxes in the maintenance of the 2013–2016 Northeast Pacific Marine Heatwave. *J. Geophys. Res.: Atmos.* **124**, 10772–10783, https://doi.org/10.1029/2019jd030780 (2019).
40. Oliver, E. C. J. et al. The unprecedented 2015/16 Tasman Sea marine heatwave. *Nat. Commun.* **8**, https://doi.org/10.1038/ncomms16101 (2017).
41. Oliver, E. C. J. et al. Longer and more frequent marine heatwaves over the past century. *Nat. Commun.* **9**, https://doi.org/10.1038/s41467-018-03732-9 (2018).
42. Kossin, J. P., Emanuel, K. A. & Vecchi, G. A. The poleward migration of the location of tropical cyclone maximum intensity. *Nature* **509**, 349–352, https://doi.org/10.1038/nature13278 (2014).
43. Liu, Y., Cai, W., Lin, X. & Li, Z. Increased extreme swings of Atlantic intertropical convergence zone in a warming climate. *Nat. Clim. Change* **12**, 828–833, https://doi.org/10.1038/s41558-022-01445-y (2022).
44. Peng, Q. et al. Surface warming–induced global acceleration of upper ocean currents. *Sci. Adv.* **8**, https://doi.org/10.1126/sciadv.abj8394 (2022).
45. Wu, L. et al. Enhanced warming over the global subtropical western boundary currents. *Nat. Clim. Change* **2**, 161–166, https://doi.org/10.1038/nclimate1353 (2012).
46. Goes, M. et al. Modulation of Western South Atlantic Marine Heatwaves by Meridional Ocean Heat Transport. *J. Geophys. Res.: Oceans* **129**, https://doi.org/10.1029/2023jc019715 (2024).
47. Behr, L. et al. The 2023 marine heatwave in the North Atlantic and the Mediterranean Sea: ocean response to atmospheric circulation. https://doi.org/10.5194/egusphere-egu24-7671 (2024).
48. Dong, L. et al. Emergence of the enhanced equatorial Atlantic warming as a fingerprint of global warming. *Nat. Commun.* https://doi.org/10.1038/s41467-025-68015-6 (2025).
49. Plecha, S. M. & Soares, P. M. M. Global marine heatwave events using the new CMIP6 multi-model ensemble: from shortcomings in present climate to future projections. *Environ. Res. Lett.* **15**, https://doi.org/10.1088/1748-9326/abc847 (2020).
50. Rashid, H. A. & Hirst, A. C. Investigating the mechanisms of seasonal ENSO phase locking bias in the ACCESS coupled model. *Clim. Dyn.* **46**, 1075–1090, https://doi.org/10.1007/s00382-015-2633-y (2016).
51. Chen, H.-C. & Jin, F.-F. The mechanism of boreal summer SSTA phase-locking in the far eastern Pacific. *npj Clim. Atmos. Sci.* **6**, https://doi.org/10.1038/s41612-023-00472-6 (2023).
52. Geng, X., Zhao, J. & Kug, J.-S. ENSO-driven abrupt phase shift in North Atlantic oscillation in early January. *npj Clim. Atmos. Sci.* **6**, https://doi.org/10.1038/s41612-023-00414-2 (2023).
53. Soden, B. J. & Vecchi, G. A. The vertical distribution of cloud feedback in coupled ocean-atmosphere models. *Geophys. Res. Lett.* **38**, n/a–n/a, https://doi.org/10.1029/2011gl047632 (2011).
54. Zelinka, M. D. & Hartmann, D. L. Why is longwave cloud feedback positive? *J. Geophys. Res.: Atmos.* **115**, https://doi.org/10.1029/2010jd013817 (2010).
55. Sun, C. et al. Western tropical Pacific multidecadal variability forced by the Atlantic multidecadal oscillation. *Nat. Commun.* **8**, https://doi.org/10.1038/ncomms15998 (2017).
56. Wang, C. Z. & Enfield, D. B. The Tropical Western Hemisphere Warm Pool. *Geophys. Res. Lett.* **28**, 1635–1638, https://doi.org/10.1029/2000gl011763 (2001).
57. Jiang, F., Seager, R. & Cane, M. A. A climate change signal in the tropical Pacific emerges from decadal variability. *Nat. Commun.* **15**, https://doi.org/10.1038/s41467-024-52731-6 (2024).
58. Wang, Y. & McPhaden, M. J. Seasonal cycle of cross-equatorial flow in the central Indian Ocean. *J. Geophys. Res.: Oceans* **122**, 3817–3827, https://doi.org/10.1002/2016jc012537 (2017).
59. Chen, Y. et al. Substantial cooling effect from aerosol-induced increase in tropical marine cloud cover. *Nat. Geosci.* **17**, 404–410, https://doi.org/10.1038/s41561-024-01427-z (2024).
60. Qiu, Z., Qiao, F., Jang, C. J., Zhang, L. & Song, Z. Evaluation and projection of global marine heatwaves based on CMIP6 models. *Deep Sea Res. II: Top. Stud. Oceanogr.* **194**, https://doi.org/10.1016/j.dsr2.2021.104998 (2021).
61. Ribes, A., Planton, S. & Terray, L. Application of regularised optimal fingerprinting to attribution. Part I: method, properties and idealised analysis. *Clim. Dyn.* **41**, 2817–2836, https://doi.org/10.1007/s00382-013-1735-7 (2013).
62. Stott, P. A. & Tett, S. F. B. Scale-dependent detection of climate change. *J. Clim.* 3282–3294 (1998).
63. Ma, X. et al. Midlatitude mesoscale thermal Air-sea interaction enhanced by greenhouse warming. *Nat. Commun.* **15**, https://doi.org/10.1038/s41467-024-52077-z (2024).
64. Yang, H. et al. Satellite-observed strong subtropical ocean warming as an early signature of global warming. *Commun. Earth Environ.* **4**, https://doi.org/10.1038/s43247-023-00839-w (2023).
65. Feng, J., Li, J., Jin, F. F., Zhao, S. & Li, J. Anthropogenic forcing drives equatorward migration of heatwave locations across continents. *Nat. Commun.* **16**, 8197 https://doi.org/10.1038/s41467-025-63558-0 (2025).
66. Ren, J., Wang, C. & Yao, Y. Spatiotemporally continuous marine heatwaves: a novel clustering approach reveals increasing frequency, duration, area, intensity, and movement distance. *Geophys. Res. Lett.* **52**, https://doi.org/10.1029/2024gl113211 (2025).
67. Bellomo, K., Clement, A. C., Murphy, L. N., Polvani, L. M. & Cane, M. A. New observational evidence for a positive cloud feedback that amplifies the Atlantic Multidecadal Oscillation. *Geophys. Res. Lett.* **43**, 9852–9859, https://doi.org/10.1002/2016gl069961 (2016).
68. Knaff, J. A. Implications of summertime sea level pressure anomalies in the Tropical Atlantic Region. *J. Clim.* 789–804 (1997).
69. Latif, M. & Keenlyside, N. S. Understanding Equatorial Atlantic interannual variability. *J. Clim.* **20**, 131–142, https://doi.org/10.1175/jcli3992.1 (2007).
70. Ma, X., Liu, W., Allen, R. J., Huang, G. & Li, X. Dependence of regional ocean heat uptake on anthropogenic warming scenarios. *Sci. Adv.* **6**, https://doi.org/10.1126/sciadv.abc0303 (2020).
71. Yun, J., Ha, K.-J. & Lee, S.-S. Impact of greenhouse warming on mesoscale eddy characteristics in high-resolution climate simulations. *Environ. Res. Lett.* **19**, https://doi.org/10.1088/1748-9326/ad114b (2024).
72. Huang, B. et al. Improvements of the Daily Optimum Interpolation Sea Surface Temperature (DOISST) Version 2.1. *J. Clim.* **34**, 2923–2939, https://doi.org/10.1175/jcli-d-20-0166.1 (2021).
73. Good, S. et al. The current configuration of the OSTIA system for operational production of foundation sea surface temperature and ice concentration analyses. *Remote Sens.* **12**, https://doi.org/10.3390/rs12040720 (2020).

74. Hersbach, H. et al. The ERA5 global reanalysis. *Q. J. R. Meteorol. Soc.* **146**, 1999–2049, https://doi.org/10.1002/qj.3803 (2020).
75. McDougall, T. J., Jackett, D. R., Feistel, R., Wright, D. G. & Griffies, S. M. Algorithms for density, potential temperature, conservative temperature, and the freezing temperature of seawater. *J. Atmos. Ocean. Technol.* **23**, 1709–1728, https://doi.org/10.1175/jtech1946.1 (2006).
76. Carton, J. A. & Giese, B. S. A Reanalysis of Ocean Climate Using Simple Ocean Data Assimilation (SODA). *Month. Weather Rev.* **136**, 2999–3017, https://doi.org/10.1175/2007mwr1978.1 (2008).
77. Mayer, J., Haimberger, L. & Mayer, M. A quantitative assessment of air–sea heat flux trends from ERA5 since 1950 in the North Atlantic basin. *Earth Syst. Dyn.* **14**, 1085–1105, https://doi.org/10.5194/esd-14-1085-2023 (2023).
78. Eyring, V. et al. Overview of the Coupled Model Intercomparison Project Phase 6 (CMIP6) experimental design and organization. *Geosci. Model Dev.* **9**, 1937–1958, https://doi.org/10.5194/gmd-9-1937-2016 (2016).
79. Danabasoglu, G. et al. The Community Earth System Model Version 2 (CESM2). *J. Adv. Model. Earth Syst.* **12**, https://doi.org/10.1029/2019ms001916 (2020).
80. Rodgers, K. B. et al. Ubiquity of human-induced changes in climate variability. *Earth Syst. Dyn.* **12**, 1393–1411, https://doi.org/10.5194/esd-12-1393-2021 (2021).
81. Hurrell, J. W. Decadal trends in the North Atlantic Oscillation: regional temperatures and precipitation. *Science* **269**, 676–679, https://doi.org/10.1126/science.269.5224.676 (1995).
82. Geng, T. et al. Increased occurrences of consecutive La Niña events under global warming. *Nature* **619**, 774–781, https://doi.org/10.1038/s41586-023-06236-9 (2023).
83. Capotondi, A. et al. Understanding ENSO diversity. *Bull. Am. Meteorol. Soc.* **96**, 921–938, https://doi.org/10.1175/BAMS-D-13-00117.1 (2015).
84. Chakravorty, S., Perez, R. C., Gnanaseelan, C. & Anderson, B. T. Revisiting the recharge and discharge processes for different flavors of El Niño. *J. Geophys. Res.: Oceans* **126**, https://doi.org/10.1029/2020jc017075 (2021).
85. Xu, H., Chen, H. & Wang, H. Detectable human influence on changes in precipitation extremes across China. *Earth's Future* **10**, https://doi.org/10.1029/2021ef002409 (2022).
86. Zhang, W., Zhou, T. & Wu, P. Anthropogenic amplification of precipitation variability over the past century. *Science* **385**, 427–432, https://doi.org/10.1126/science.adp0212 (2024).
87. Sun, Y. et al. Rapid increase in the risk of extreme summer heat in Eastern China. *Nat. Clim. Change* **4**, 1082–1085, https://doi.org/10.1038/nclimate2410 (2014).
88. Ding, M. et al. Overestimated Eddy Kinetic energy in the Eddy-Rich regions simulated by Eddy-Resolving Global Ocean–Sea Ice Models. *Geophys. Res. Lett.* **49**, https://doi.org/10.1029/2022gl098370 (2022).

Acknowledgements
This work was supported by the National Key Research and Development Program of China (2023YFF0805100, 2023YFC3107702, 2024YFF0808900), National Natural Science Foundation of China (42206218), the Project of Southern Marine Science and Engineering Guangdong Laboratory (Zhuhai) under Contract No. SML2024SP023.

Author contributions
J.F. designed the original ideas of the study and structured the paper. X.L.J. performed the data analysis and wrote the original manuscript, in discussion with J.F., J.P.L., X.R.C., F.K., X.C.L., and R.Q.D. All authors contributed to the interpretation of the results and improvement of the manuscript.

Competing interests
The authors declare no competing interests.

Additional information
Supplementary information The online version contains supplementary material available at https://doi.org/10.1038/s41612-026-01426-4.

Correspondence and requests for materials should be addressed to Juan Feng.